

Many-Body Neural Network Wavefunction for a Non-Hermitian Ising Chain

Lavoisier Wah,^{1,2,*} Remmy Zen,^{1,†} and Flore K. Kunst^{1,2,‡}

¹*Max Planck Institute for the Science of Light, 91058 Erlangen, Germany*

²*Department of Physics, Friedrich-Alexander-Universität Erlangen-Nürnberg, 91058 Erlangen, Germany*

(Dated: June 16, 2025)

Non-Hermitian (NH) quantum systems have emerged as a powerful framework for describing open quantum systems, non-equilibrium dynamics, and engineered quantum optical materials. However, solving the ground-state properties of NH systems is challenging due to the exponential scaling of the Hilbert space, and exotic phenomena such as the emergence of exceptional points. Another challenge arises from the limitations of traditional methods like exact diagonalization (ED). For the past decade, neural networks (NN) have shown promise in approximating many-body wavefunctions, yet their application to NH systems remains largely unexplored. In this paper, we explore different NN architectures to investigate the ground-state properties of a parity-time-symmetric, one-dimensional NH, transverse field Ising model with a complex spectrum by employing a recurrent neural network (RNN), a restricted Boltzmann machine (RBM), and a multilayer perceptron (MLP). We construct the NN-based many-body wavefunctions and validate our approach by recovering the ground-state properties of the model for small system sizes, finding excellent agreement with ED. Furthermore, for larger system sizes, we demonstrate that the RNN outperforms both the RBM and MLP. However, we show that the accuracy of the RBM and MLP can be significantly improved through transfer learning, allowing them to perform comparably to the RNN for larger system sizes. These results highlight the potential of neural network-based approaches—particularly for accurately capturing the low-energy physics of NH quantum systems.

I. INTRODUCTION

Traditional quantum mechanics relies on Hermitian Hamiltonians to ensure real eigenvalues and unitary time evolution. However, non-Hermitian (NH) quantum mechanics has emerged as a powerful framework to describe open quantum systems, where interactions with the environment may lead to energy dissipation and gain [1, 2]. A particularly intriguing subclass of non-Hermitian systems consists of those obeying parity-time (PT) symmetry, where the Hamiltonian remains invariant under simultaneous spatial reflection and time-reversal operations [3]. Such systems exhibit real eigenvalues in the unbroken PT -symmetric phase, and undergo a phase transition through an exceptional point (EP), where two or more eigenvalues and their corresponding eigenvectors coalesce. Beyond this point, the system enters the broken PT -symmetric regime, where eigenvalues become complex [4]. This rich phenomenology has inspired studies across condensed matter physics, quantum optics, and cold-atom systems [2, 4–10].

Recent advances have extended NH physics from single-particle systems to many-body quantum systems, unveiling novel exotic phenomena and a richer understanding of EPs and the NH skin effect leading to novel phases [11], unconventional localization and distinct quantum criticality [12–15]. These developments have been explored in various contexts, including NH extensions of the transverse field Ising model (TFIM),

where complex interactions lead to unconventional symmetry breaking and dynamical properties [14, 16–18]. Despite significant progress in theoretical formulations, an efficient numerical method to determine the ground-state properties of non-Hermitian many-body systems remains an open challenge due to the exponential scaling of the Hilbert space as well as the instabilities induced by the emergence of EPs.

The application of artificial intelligence and machine learning techniques in quantum many-body physics has provided innovative approaches to studying strongly correlated systems [19–21]. Neural-network-based variational wavefunctions or neural quantum states (NQSs), such as restricted Boltzmann machines (RBMs), multilayer perceptrons (MLPs), and recurrent neural networks (RNNs) have demonstrated remarkable success in approximating ground states of complex quantum systems [22–26]. By parameterizing the wavefunction with a neural-network model, it can capture entanglement and correlation structures efficiently, making them well-suited for studying quantum phases and transitions [22, 23, 27]. However, NQSs has so far been restricted to Hermitian many-body systems and their application to NH many-body physics offers a promising alternative to traditional numerical techniques, such as exact diagonalization (ED) and tensor network methods, which become computationally prohibitive for large system sizes. Very recently, these techniques have only been applied to study NH fermionic systems with real spectrum using the RNN [28]. Here, we propose to further the study to the realm of many-body *bosonic* NH systems with a *complex spectrum*, which is the “raison d’être” of this paper. Our goal is to develop fast and efficient algorithms capable of capturing the many-body wavefunction of bosonic NH

* lavoisier.wahkenounouh@mpl.mpg.de

† remmy.zen@mpl.mpg.de

‡ flore.kunst@mpl.mpg.de

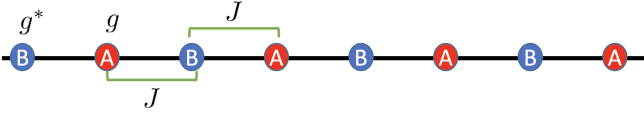


Figure 1: **1D Ising chain in a staggered magnetic field.** A (red) and B (blue) represent the sublattices in which spin-1/2 particles occupy the odd and even positions, respectively. The complex field g (g^*) is applied to the A (B) sublattices. Neighboring spins are coupled via the coupling constant J .

systems and propose a method to investigate their ground state.

Extending many-body neural-network wavefunctions to NH systems enables the exploration of exotic ground states, particularly in PT -symmetric models, where standard Hermitian variational techniques may fail. This work aims to develop and apply a neural-network-based variational Monte Carlo (VMC) method to study the ground-state properties of a PT -symmetric non-Hermitian TFIM with complex spectrum. The TFIM is the perfect model to test VMC in NH systems because the model can be solved analytically [16, 17]. Using our numerical techniques, we not only find that our results are in perfect agreement with ED but also provide new insights into metastable states that are not fully accessible with ED as discussed later.

In what follows, we present our model in Sec. II and discuss the concept of the ground state in NH systems. In Sec. III, we demonstrate how to recover the ground state for our model. We then show in Sec. IV how transfer learning (TL) can enhance the performance of the neural networks. In Sec. V, we study the unbroken-to-broken phase transition and show the emergence of EPs. Finally, our results are summarized in Sec. VI.

II. MODEL AND NON-HERMITIAN SYMMETRY

A. Hamiltonian

The model of interest consists of a one-dimensional (1D) quantum Ising chain of N spin-1/2 particles on two sublattices A and B coupled via a spin coupling J and subject to a complex, staggered magnetic field that introduces non-Hermiticity into the system (see Fig. 1). The NH field is chosen so that $g = \eta + i\xi$ is applied perpendicularly to the spins on sublattice A (red) and $g^* = \eta - i\xi$ to the spins on sublattice B (blue) with $\eta, \xi \in \mathbb{R}$. The Hamiltonian describing such a system is given by

$$H = -J \sum_{j=1}^N \sigma_j^z \sigma_{j+1}^z - g \sum_{j \in A} \sigma_j^x - g^* \sum_{j \in B} \sigma_j^x, \quad (1)$$

where σ_j^z and σ_j^x are Pauli matrices. This setting imposes that any gain due to the imaginary part of the magnetic field, $+\xi$, is balanced by an equivalent loss, $-\xi$. Moreover,

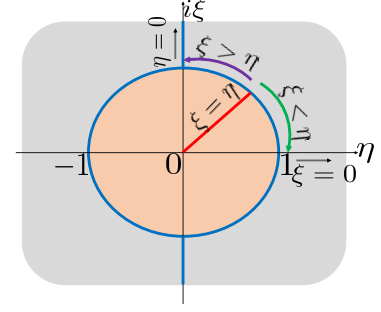


Figure 2: **Phase diagram of the ground state of the NH TFIM.** The orange region is the ferromagnetic phase, while the gray region represents the paramagnetic phase with the blue line being the set of critical points at which the quantum phase transition occurs. The plot represents different regimes of the system namely, the regime of weak non-Hermiticity $\xi < \eta$ (green arrow), strong non-Hermiticity $\xi > \eta$ (violet arrow), complete non-Hermiticity $\eta = 0$, equal contribution of the real and imaginary parts of g (red line), and complete Hermiticity $\xi = 0$.

the real part of the field, η , behaves like a standard transverse field, driving fluctuations between spin states. This model is PT -symmetric. The action of the parity operator P , which amounts to spacial reflection, is written as $P\sigma_j^\nu P^{-1} = \sigma_{N-j+1}^\nu$. The time-reversal operator T acts as $TiT^{-1} = -i$, and $T\sigma_j^\nu T^{-1} = \sigma_j^\nu$ with $\nu = x, z$, i.e., it leaves the spin on each site invariant. One can then show that $[PT, H] = 0$. Unless stated otherwise, we shall work in the regime where $J = 1$ and periodic boundary conditions (PBCs) are considered, i.e., $\sigma_j^\nu = \sigma_{j+N}^\nu$. Under these conditions the model is immediately in the PT -broken phase (see Appendix A).

The phase diagram of the system in the complex plane is obtained by plotting the energy density as a function of the components of the field. A projection of this phase diagram in the $(\eta - i\xi)$ -plane is depicted in Fig. 2. As discussed in Ref. [17], the non-Hermiticity has the effect of shrinking the paramagnetic phase (gray region). Indeed, the presence of non-Hermiticity introduces a perturbation in the system's dynamics. Since in the paramagnetic phase, the magnetic field tends to align all the spins in its direction, and thus leading to a more ordered phase, the non-Hermiticity perturbs this ordering and leads to more disordered behavior that suppresses the stabilizing quantum fluctuations induced by the field in the ferromagnetic phase (orange region).

The non-Hermitian Hamiltonian in Eq. (1) can be solved analytically in an analogous fashion to the Hermitian case. We refer to Refs. [16, 17] for detailed calculations.

B. Ground state of non-Hermitian systems

Likewise to a conventional (Hermitian) system, the ground-state (indexed with 0) average of any physical observable in NH systems can be obtained by “sandwiching” the Hamiltonian with some eigenstates. In this

particular case, one of the most used formulations is the biorthogonal formalism [29, 30], which can be understood as a NH analogue to the quantum mixed estimator in Hermitian physics. As such, for a given observable \mathcal{O} one has

$$\langle \mathcal{O} \rangle = \frac{\langle \Psi_{0,L} | \mathcal{O} | \Psi_{0,R} \rangle}{\langle \Psi_{0,L} | \Psi_{0,R} \rangle}, \quad (2)$$

where $|\Psi_{0,R}\rangle$ and $\langle \Psi_{0,L}|$ are the right and left ground-state wavefunctions of H , respectively, satisfying the biorthonormal product

$$\langle \Psi_{i,L} | \Psi_{j,R} \rangle = \delta_{i,j}. \quad (3)$$

Following this prescription, for a given spin configuration $\mathbf{x} = \{x_1, x_2, \dots, x_N\}$, we compute the local energy of the system as follows

$$E_{\text{loc}}(\mathbf{x}) = \frac{\langle \mathbf{x} | H | \Psi_{0,R} \rangle}{\langle \mathbf{x} | \Psi_{0,R} \rangle} = \frac{\langle \Psi_{0,L} | H | \mathbf{x} \rangle}{\langle \Psi_{0,L} | \mathbf{x} \rangle}. \quad (4)$$

Note that the choice of whether to use the left or right eigenstate to compute E_{loc} does not matter since this formulation allows the Hamiltonian to produce the same energy when acting to the left or to the right, which we show in Appendix B. This formulation is particularly important in NH systems and we shall subsequently discuss its relevance.

Before going into more detail on how to recover the true ground state of a NH system, it is important to first discuss what this means for a NH systems. While some works provide a possible way to get to the ground state of a NH model [31, 32], the concept of a ground state is in principle not well defined and may be subject to many interpretations due to the complex energy spectrum and the lack of a variational principle. In Hermitian systems, the ground-state wavefunction is the eigenstate corresponding to the lowest energy eigenvalue of the Hamiltonian, which is always real due to Hermiticity. In NH systems, the eigenvalues of the Hamiltonian can be complex valued, meaning there is no universally defined lowest energy in the conventional sense. Instead, the ground state can be defined in terms of eigenstates with the smallest real part, the smallest magnitude, the smallest imaginary part of the eigenvalues, or any other possible combination of these scenarios. Here, we propose to find the many-body wavefunction that minimizes the real part of the energy expectation value. We will see that the ground-state energy of the NH TFIM is in fact purely real without any imaginary contribution as is also found in Refs. [16, 17].

An additional layer of complexity in the choice of the ground-state wavefunction is that the wavefunctions are handed (left, right), and one needs to choose which eigenstate to use in order to compute the local energy. The latter can be easily solved by using our formulation of the local energy in Eq. (4), which becomes the true ground-state energy provided the corresponding ansatz (many-body eigenstate), $\Psi_{0,R/L}$, is the ground-state wavefunction of the Hamiltonian. This formulation then enables

us not to care about whether we use the right or left wavefunction.

III. GROUND STATE WITH NEURAL NETWORKS

Here, we use a neural network as an ansatz to a many-body wavefunction, that is given an input configuration \mathbf{x} , it outputs $\Psi(\mathbf{x})$. We use the variational principle by using Monte Carlo sampling to sample several configurations \mathbf{x} then computing and minimizing the average local energy given in Eq. (4) (see Appendix B). As we are looking for the state with lowest real energy, we use an algorithm that minimizes the real part. We note, however, that our algorithm can be easily adapted to look for states with largest real part, largest or smallest imaginary part, largest or smallest absolute value or even a certain combination of real and imaginary parts of the energy. As such, the algorithm can thus be readily adapted and applied to systems with a fully complex ground-state energy.

Since NH effects can lead to numerical instabilities during optimization, especially for large systems or strongly NH regimes, we restrict our simulation to the weak NH regime ($\xi < \eta$), so we set $\xi = \eta/10$ everywhere in this paper, and introduce a regularization factor α in the loss function.

By minimizing the real part of energy, we identify the eigenstate that is energetically stable (lowest real part). As this state has a disappearing imaginary part, it is also dynamically stable. This eigenstate represents the ground state (in a generalized sense) of the NH system. Our approach acts as a physical filter that only focuses on the physically relevant spectrum instead of considering all state—many of which are noise in practice—as in the case of ED. A summarized general algorithm describing the aforementioned implementation for the RNN, RBM, and MLP can be found in Appendix B. It is worth emphasizing that this procedure is naturally also valid for the unbroken PT -symmetric regime, where all the local energies are real.

A. Non-Hermitian many-body neural network wavefunctions

Recent advances in machine learning have provided powerful tools for studying quantum many-body systems, particularly through neural network-based variational wavefunctions [22, 33–38]. Among these, RNNs [23, 39, 40], RBMs [41–43], and MLPs [38, 44–46] have emerged as effective representations for approximating quantum states. These architectures offer distinct advantages: RBMs are energy-based models made of a dense single-layer feed-forward network [47] that capture non-trivial correlations with relatively few parameters, while MLPs provide a flexible framework for function approx-

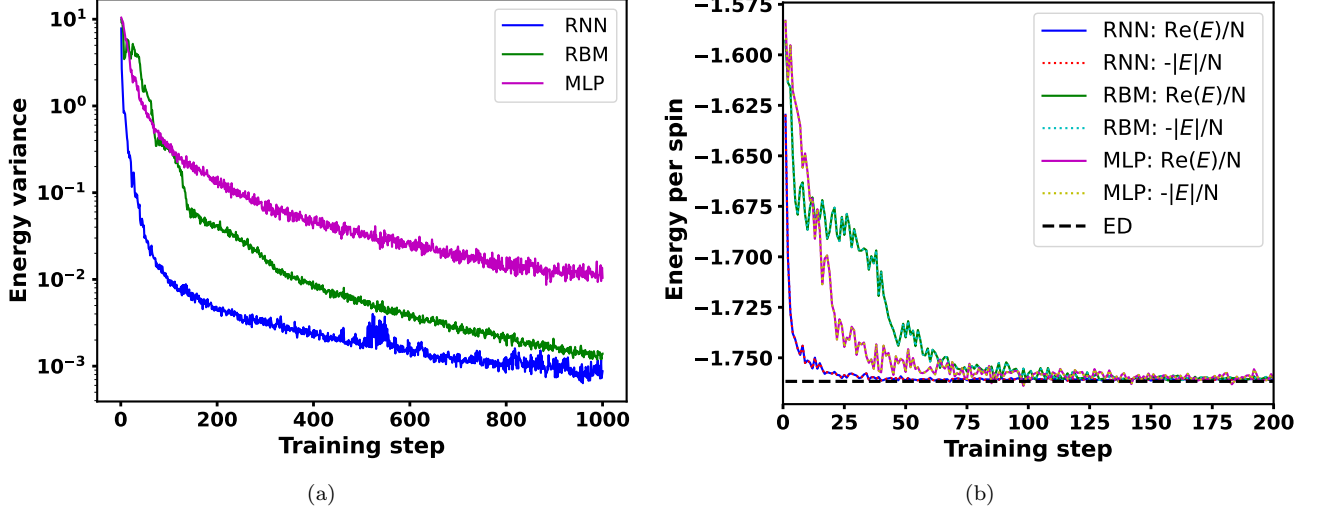


Figure 3: **Neural network architectures versus exact diagonalization.** First, we represent (a) the local energy variance of the real part of the average local energy for the RNN (blue), RBM (green), and the MLP (magenta). The RNN converges faster than the RBM and the MLP. Then, we simulate (b) the ground-state energy of the model for the staggered magnetic field with the RNN (blue), RBM (green), and MLP (magenta). All neural network algorithms recover the true ground-state energy predicted by ED (black dashed line). We also plot the negative absolute value of the energy for the RNN (dashed red), RBM (dashed cyan) and, MLP (dashed yellow) for comparison. In both plots, we set $\eta = 1.6$ and $\xi = 0.16$.

imation. RNNs, on the other hand, are particularly well-suited for sequential data and have demonstrated remarkable success in modeling quantum wavefunctions. A key motivation behind this framework is that this architecture enables autoregressive sampling. As a result, new independent samples can be generated in a single network evaluation, eliminating the need for Markov chain Monte Carlo, which may suffer from long autocorrelation and thermalization times [47]. By leveraging these methods, we aim to construct NH many-body wavefunctions and assess their ability to capture the system’s critical behavior to simulate the ground-state properties of the model and compute the corresponding physical observables.

In this section, we simulate the ground state of the model using an RNN, an RBM, and an MLP. We benchmark our results against ED and the high-order series expansion (SE) derived in Ref. [16] for the low- ($\eta/J, \xi/J \ll 1$) and high-field ($\eta/J, \xi/J \gg 1$) limits that we numerically extrapolated (see Appendix C) to capture the intermediate-field regime. In each of the neural network architectures, we enforced PT symmetry on the many-body ansatz following the prescription in Appendix D. Although we enforce this symmetry on our original ansatz, the main idea is to have a neural network that can capture such a symmetry if present in the system at the beginning of the simulation [as it is the case when considering open boundary conditions (OBCs)]. However, it is instructive to note that the neural network breaks this symmetry as soon as we enter the broken regime fully consistent with the breakdown of PT symmetry for wavefunctions in this phase. A general overview of the algorithms can be found in Appendix B, and the

parameters used for all simulations in this paper are summarized in Appendix E.

First, we plot and compare the energy variance for each architecture, as shown in Fig. 3(a). The results indicate that the energy estimates exhibit low fluctuations and steadily converge toward a well-defined value for each architecture. We see that the RNN achieves a stable energy estimate more rapidly than both the RBM and MLP (as we in general expect for a Hermitian system as well) suggesting that it is more efficient in capturing the ground-state properties of the system.

We also analyze the evolution of the local energy during the training process for each architecture, cf. Fig. 3(b). As predicted by the variance, the RNN converges more rapidly. In the broken PT -symmetry regime, the energies mostly come in complex conjugate pairs. As a result, averaging cancels out the imaginary components, making the real part of the energies effectively equivalent to taking the absolute value as we confirm in Fig. 3(b), where the negative sign is introduced to indicate the ground-state energy has a negative value. Although in the broken phase, the fact that one observes an equivalence between the real part and the magnitude of the energy suggests that we are in a region where only a few states break the PT symmetry, and so we are moving toward the unbroken region where we observe a “real-like” behavior of the energy. As a result, we are capturing the dynamics of the system close to an exceptional point.

Furthermore, we investigate the ground-state energy per spin for each neural network architecture as a function of η and construct a corresponding phase diagram, cf. Fig. 4. In the small-system-size regime, where ED is

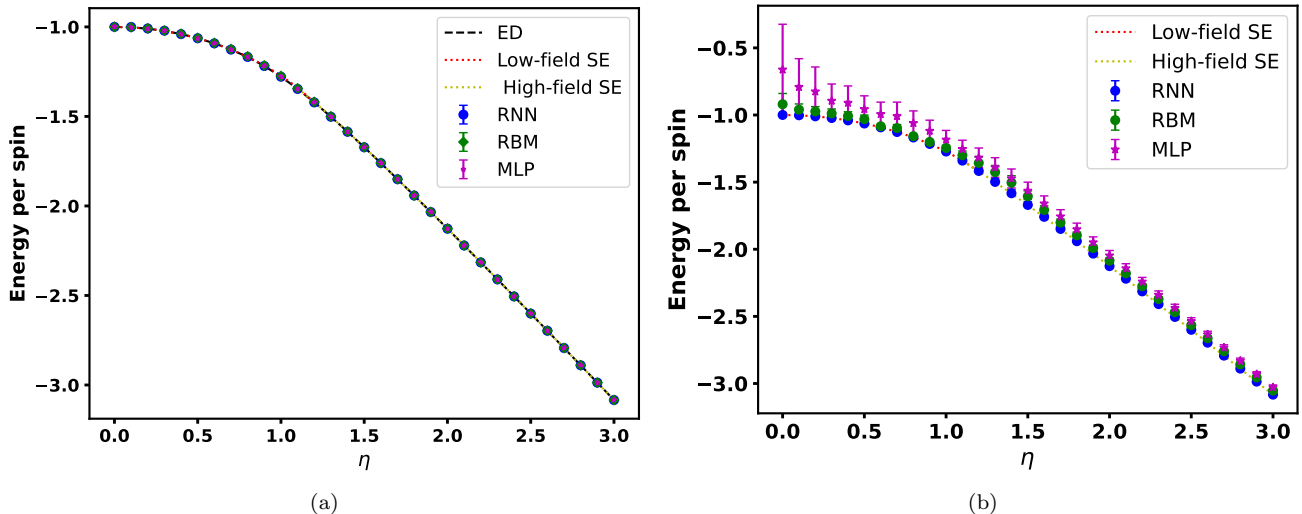


Figure 4: **Ground-state energy per spins.** We plot the average ground-state energy per spin against the η for (a) the extrapolated high-order SE, where we depict both the low-field (dotted red) and the high-field (dotted yellow) regimes. We make use of an RNN (blue circles), an RBM (green circles) and an MLP (cyan stars) and compare the results with ED (dashed black line). The error bars are smaller than the data points and $N = 10$. Beyond ED, for (b) $N = 100$, we also compute the energy per spin for the RNN (blue circles), the RBM (green circles) and the MLP (magenta circles), and compare the result with the extrapolated higher-order SE (red and yellow dotted lines). The RNN is more efficient than the RBM and the MLP. $\xi = 0.16$ in both plots.

feasible ($N = 10$), all neural network architectures perform similarly, and their results closely match those obtained from ED and the extrapolated high-order SE as shown in Fig. 4(a). However, for larger system sizes, beyond the reach of ED ($N = 100$), Fig. 4(b), the autoregressive nature of the RNN allows it to effectively capture the system's dynamics, whereas the RBM and MLP struggle to achieve the same level of accuracy. This suggests that the RNN is robust and thus the most suitable architecture for our study (which is in general true for Hermitian models as well). Nevertheless, we later show that one can further improve the performances of all our neural network architectures using TL.

B. Recurrent neural network versus series expansion around criticality

In Ref. [16], Lea *et al.* employed the high-order SE to investigate the ground state in both the low- and high-field regimes with remarkable accuracy. Given that the RNN has demonstrated superior performance among the tested neural network architectures, we compare its accuracy near the transition point to that of the SE method. Our results indicate that, around this critical region, the RNN more effectively captures the system's dynamics than the high-order SE approach. The relative error obtained with both methods is illustrated in Fig. 5. This finding suggests that our algorithm is robust and that the RNN is a promising choice for studying NH quantum systems.

In addition, an SE is inherently limited to perturba-

tive corrections around a known limit (low- and high-field) [16]. In contrast, an RNN-based, or any neural network-based, variational ansatz in general can be optimized globally, allowing it to capture the full phase diagram, including regimes where perturbation theory fails, e.g., near exceptional points or in strong anti-Hermitian fields. Also, the RNN allows efficient sampling of system configurations, which enables direct computation of physical observables, such as magnetization and entanglement entropy, across the entire phase diagram, whereas an SE typically focuses on specific quantities (like the ground-state energy and the energy gap) and only in particular limits. Furthermore, the high-field gap in SE is inaccessible perturbatively due to complex energy eigenvalues and the presence of exceptional lines [16]. Since an RNN-based approach works by direct optimization of a trial wavefunction, it can learn the structure of eigenstates even in these non-trivial regions. Moreover, the RNN ansatz is particularly powerful for capturing long-range correlations in 1D quantum systems. This is crucial for PT -symmetric models, where NH effects can induce complex correlation patterns that standard perturbative methods may not fully describe. So, the RNN implementation provides a more complete picture of PT -symmetric phase transitions beyond what the SE method can achieve and offers much more flexibility. Nevertheless, the SE outperforms the RNN at high- and low-field limits, and allows to access the functional approximate form of the ground-state energy.

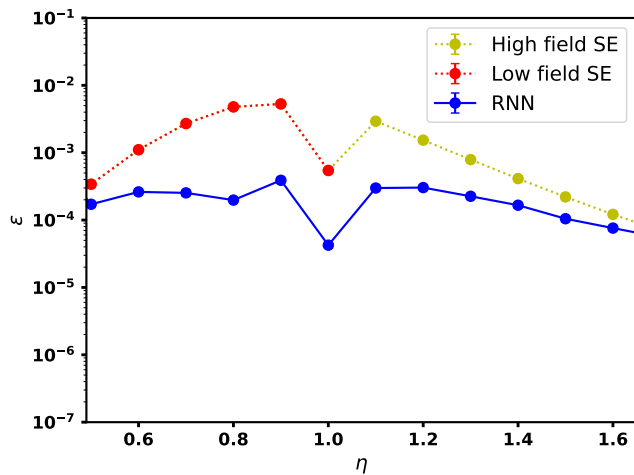


Figure 5: **Relative errors on RNN and SE.** We compute the relative errors $\epsilon_{RNN} = |\text{Re}(E_{ED}) - \text{Re}(E_{RNN})|/|\text{Re}(E_{ED})|$ (blue) and $\epsilon_{SE} = |\text{Re}(E_{ED}) - \text{Re}(E_{SE})|/|\text{Re}(E_{ED})|$ (red and yellow) for $N = 10$ and $\xi = 0.16$, where E_{RNN} and E_{SE} are the ground-state energies obtained with the RNN and the extrapolated SE, respectively. The error bars are smaller than the data points.

IV. TRANSFER LEARNING AND QUANTUM PHASE TRANSITION

Previously, we analyzed the behavior of the energy per spin as a function of η for different system size. Building on this, we now turn our attention to phase transitions in magnetization, $\langle m \rangle = N^{-1} \sum_{i=1}^N \langle \sigma_i^z \rangle$, which serves as an order parameter. Additionally, we aim to enhance the efficiency of our NQS using TL.

Humans naturally transfer knowledge between tasks by recognizing and applying relevant information from past experiences to new situations. The closer a new task is to something we have learned before, the easier it is to master. This principle is the same as the one used in TL [48] in contrast to traditional machine learning algorithms, which typically focus on isolated tasks. TL aims to bridge this gap by developing methods that leverage knowledge from one or more source tasks to enhance learning in a related target task. From a physical perspective, one would anticipate a connection between the wavefunctions of systems that share the same parameter values but differ in size, as if they represent the same system observed at varying length scales [49–51]. Here, we investigate TL strategies inspired by this principle, and show that they outperform a “cold-start” approach in terms of both effectiveness and efficiency.

First, we compute the magnetization within ED, where all neural network architectures perform relatively well, though the RBM and MLP exhibit some errors as shown in Figs. 6(a-c). For larger system sizes ($N = 100$), only the RNN recovers the magnetization. However, for each system size, the algorithm must be “cold-started” making the simulations computationally expensive. To address this, we propose reusing the same samples and weights

from the initial value of η (that is $\eta = 3.0$) to simulate the system at a later value of η (that is $\eta = 2.9$) (see Fig. 6), and then fine tune the neural network model. This process is repeated until $\eta = 0.0$.

By employing TL, we first demonstrate that the performance of both the RBM and MLP is significantly improved allowing them to simulate larger system sizes as shown in Figs. 6(h,i). Furthermore, TL enhances the efficiency of all architectures, making the simulations faster and more effective, cf. Figs. 6(j-l). It can be seen that the energy per spin with transfer learning always starts lower than the energy per spin without transfer learning. This improvement is particularly evident for the MLP and RBM, where the TL-based algorithm converges more rapidly. In general, incorporating TL across all architectures reduces the initial computational cost, as the algorithm benefits from the prior knowledge encoded in the reused weights and biases.

In the standard Hermitian TFIM, the phase transition occurs between the ordered (ferromagnetic) phase, where the spins align and lead to a non-zero magnetization, and the disordered (paramagnetic) phase, where the spins become disordered and the magnetization approaches zero [52]. In our case, the situation is more complex due to the PT symmetry, and the phase transition could also refer to an abrupt change in the eigenstates of the model [17], i.e., they may coalesce, as we will discuss more in detail later. However, the magnetization can still serve as a signature of the ordering or quantum phase transition that is the transition between the ordered and disordered phases. This allows us to locate the critical point where this transition occurs ($\eta_c = 1$) as shown in Figs. 6(a-i).

V. UNBROKEN-TO-BROKEN PHASE TRANSITIONS: EXCEPTIONAL POINTS

In non-Hermitian systems, particularly those with PT symmetry, the concept of phase transitions becomes richer and can be extended compared to Hermitian systems. Earlier, we used neural networks to show a phase transition in the magnetization of the system from the ferromagnetic to the paramagnetic phase and vice-versa. In this section we study another type of phase transition, which is no longer related to the spin alignment in the system, but rather related to a sudden change in the eigenstates of the system. This type of phase transition is called the *unbroken-to-broken* phase transition, which directly relates to the PT symmetry in the model. As PT symmetry is immediately broken for the NH TFIM under PBCs (see Appendix A), we consider OBCs in this section. Moreover, since the study of this phase transition requires access to the full energy and eigenstate spectra, for now we focus on using ED, but one can in principle extend our approach and use neural networks. However, it is instructive to note that such an extension in neural networks has so far only been successful for low-lying ex-

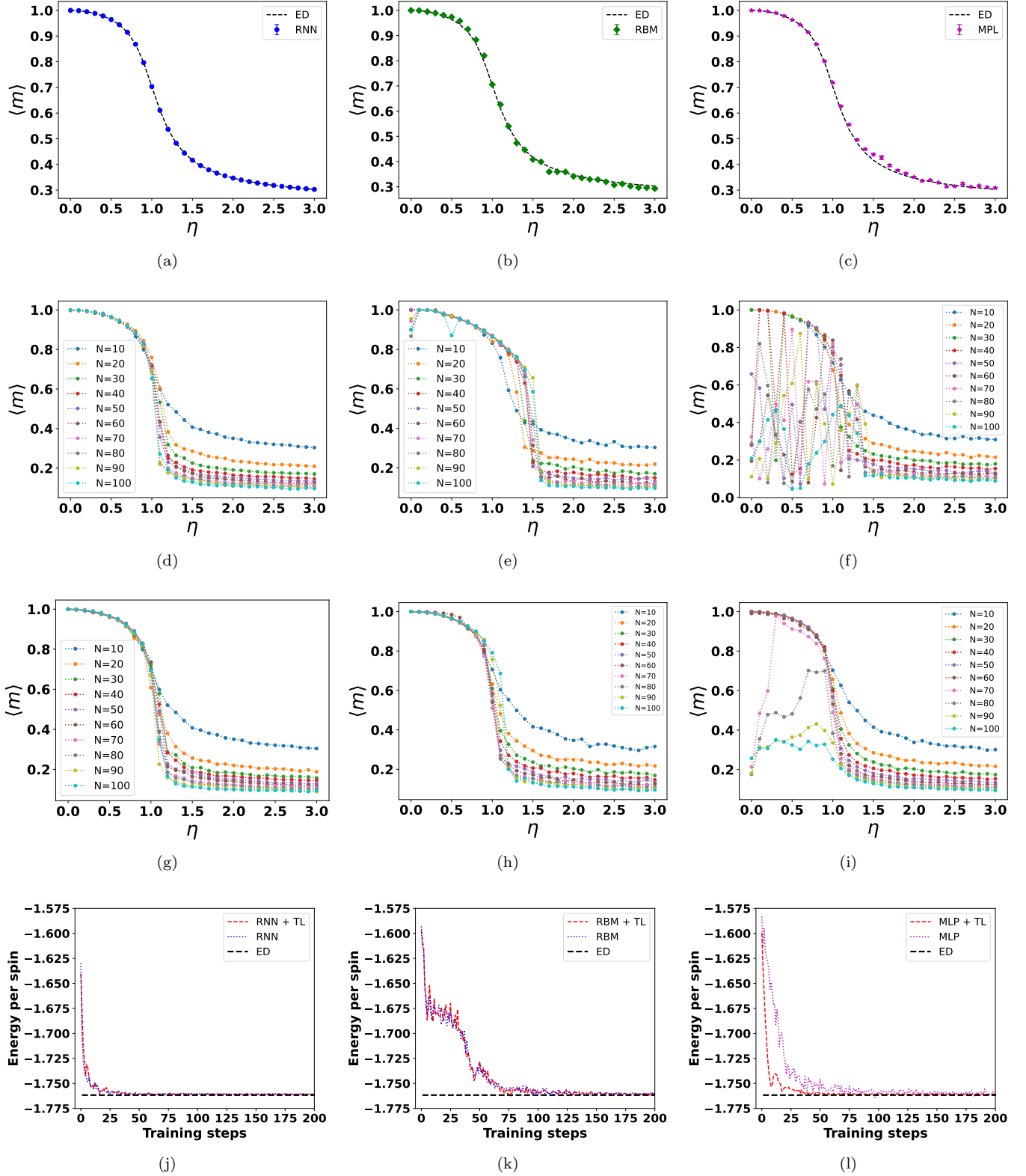


Figure 6: **Transfer learning.** We plot the magnetization of the system $\langle m \rangle$ for different system sizes across various neural network architectures. The first column corresponds to simulations using the RNN, while the second and third columns represent results from the RBM and MLP, respectively. The first row (a-c) shows the magnetization for $N = 10$ and $\eta = 1.6$ compared to ED. The second row (d-f) presents the magnetization for different system sizes for each architecture, while the third row (g-i) incorporates transfer learning to enhance performance. The final row (j-l) illustrates the training process for each architecture, both with and without transfer learning for $N = 10$ and $\eta = 1.6$ compared to ED. The quantum phase transition occurs at $\eta = 1$.

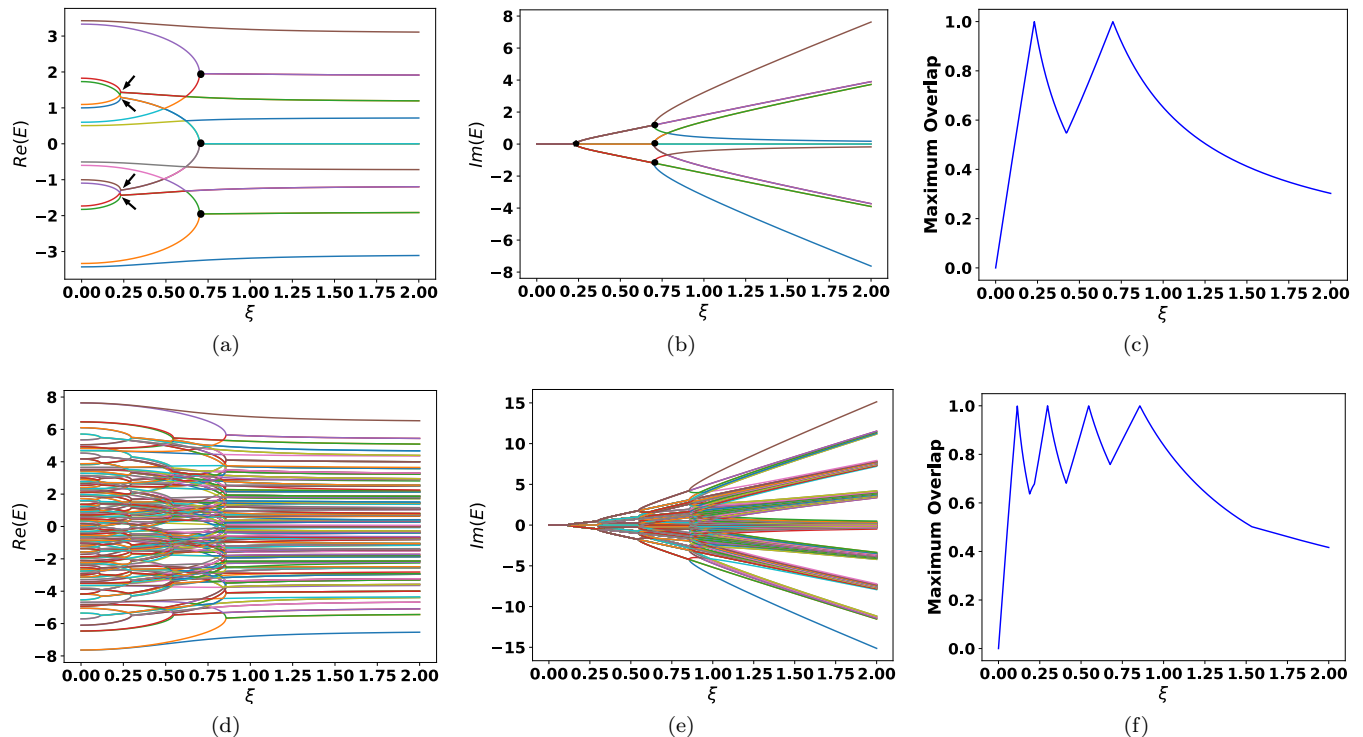


Figure 7: **Unbroken-to-broken phase transition: Exceptional points.** We analyze the (a) real and (b) imaginary parts of the energy spectrum of the system and observe the emergence of exceptional points [highlighted with black dots and arrows in (a)]. We consider $N = 4$ and $\eta = 0.5$ and the coloring is determined by the order in which the bands appear. To effectively confirm that these points are EPs, we analyze the (c) maximum overlap between all eigenstates and observe two peaks corresponding to the location of EPs. Likewise for (d-f) with $N = 8$, one observes the emergence of EPs at four different values of ξ . OBCs are considered in this figure.

cited states in Hermitian systems [53–55], and one cannot access the full functional form of the eigenstates, which are required to study unbroken-to-broken phase transitions.

A. Unbroken-to-broken phase transition

Here, the *unbroken-to-broken* phase transition refers to a transition between two regimes defined by the behavior of the eigenvalues and crucially the eigenvectors of the system’s Hamiltonian. When the system’s Hamiltonian maintains unbroken PT symmetry, the eigenvalues of the system’s Hamiltonian are real [see Fig. 7(a)], and the eigenvectors are invariant under the PT -symmetric operation. The realness of the eigenvalues is analogous to the ordered phase in traditional Hermitian systems, where all eigenstates correspond to well-defined physical states. In this phase, the system behaves as expected in terms of its observable quantities, like magnetization or energy, and exhibits characteristics similar to conventional quantum systems. Changing the system’s parameters may lead to a breakdown of PT symmetry enabling the system to enter the broken phase, where the eigenvalues of the system’s Hamiltonian become complex or purely imaginary [see Fig. 7(b)] [3], and eigenvectors are

no longer invariant under PT symmetry. The transition from real to complex eigenvalues marks the crossing from the unbroken to the broken phase and this crossing passes through an EP. The broken PT -symmetry phase is more akin to a dissipative or unstable regime, where the system may exhibit some exotic behaviors including the formation of additional EPs.

From Figs. 7(a, b), we observe that at specific points, pairs of eigenstates merge with a characteristic square-root behavior indicating the presence of an EP. At these EPs, the two eigenvalues become degenerate and the corresponding eigenvectors also coalesce, which is a defining feature of NH degeneracies. Immediately beyond this coalescence, the energy spectrum transitions from being entirely real to having complex eigenvalues, which is the hallmark of PT -symmetry breaking. This transition signifies that the system has entered the broken PT phase.

B. Exceptional points

So far, we have been working under PBCs, but now we move to OBCs. Under these boundary conditions, we investigate the emergence of EPs arising during the *unbroken-to-broken* phase transition.

The presence of these EPs is first hinted at by the

square-root singularity, which is a universal feature of NH phase transitions and is linked to the criticality of the system at the transition point. It can be further confirmed by analyzing the overlap between eigenstates. Indeed, we compute an “all-to-all” dot product between all pairs eigenstates of the system \mathbf{v}_i and \mathbf{v}_j (where $i \neq j$) and calculate their overlaps. The maximum overlap is the largest value among all these pairwise overlaps

$$\text{max_overlap} = \max_{i \neq j} |\mathbf{v}_i^\dagger \mathbf{v}_j|. \quad (5)$$

At an EP, two or more eigenvectors become linearly dependent, meaning they “merge” or coalesce. As a result, the overlap between these eigenvectors reaches exactly one at the EP. Away from an EP, the eigenvectors remain linearly independent, and the maximum overlap is strictly less than 1, as shown in Fig. 7(c). This behavior can be summarized as follows:

$$\begin{aligned} \text{max_overlap} &= 1 && \text{(at an EP),} \\ \text{max_overlap} &< 1 && \text{(away from an EP).} \end{aligned} \quad (6)$$

From Fig. 7(c), we observe two distinct peaks where the maximum overlap reaches 1. These peaks appear precisely at the locations of the eigenvalue degeneracies thus confirming they are indeed EPs. The first peak of the maximum overlap corresponds to the position of four superimposed EPs, while the second peak marks the location of the remaining three EPs. The same observation can be made for a system with $N = 8$, cf. Figs. 7(d-f).

VI. CONCLUSION

In this work, we demonstrate how conventional machine learning and artificial intelligence techniques can be extended to study NH systems. We go beyond previous studies using neural networks to study NH systems by considering a model with a complex spectrum. To study these models, we explicitly address the challenge posed by biorthogonality through formulating the local energy in a way that is independent of whether one works with the left or right eigenstate. We then show that for small system sizes, the RNN, RBM, and MLP architectures successfully recover the ground state with comparable accuracy. Their performance is benchmarked against ED and a high-order SE extrapolation, which we use to capture the system’s dynamics in the intermediate field regime. Despite the high accuracy of SE, we find that near criticality, the RNN demonstrates superior performance as one will expect (in general) for a Hermitian system. For larger system sizes, the RNN outperforms both the RBM and MLP, while achieving accuracy comparable to SE. However, unlike SE, the RNN allows for efficient computation of physical observables. Moreover, we study the magnetic phase transitions and show that employing TL enhances the performance of all neural network architectures. In particular, TL significantly accelerates the convergence of RBM and MLP, enabling them

to compute magnetization at larger system sizes with improved accuracy. Finally, we use ED to investigate the unbroken-to-broken phase transition of the system under OBCs and the emergence of EPs. We extend the technique based on computing the maximum overlap of the “all-to-all” dot product between eigenstates used in Refs. [56, 57] to many-body NH systems and enable the identification of EPs.

We note that the algorithm developed in this work can be straightforwardly adapted to find different states. While we are interested in finding the state with the lowest real energy in this work, one may instead be interested in finding, e.g., excited states such as the state with the largest imaginary energy. In this case, instead of defining the loss function \mathcal{L} in terms of the real part of the eigenvalues, one can define it in terms of the imaginary parts.

Another extension of this work is to study systems beyond non-interacting PT -symmetric models. While our method is tailored here to focus on the real part of the spectrum, it can be straightforwardly tailored to take the complete complex picture into account. The main challenge for such an extension actually lies in the ansatz of the many-body wavefunction, which should then in principle obey a different symmetry. Additionally, adding interactions or moving to higher dimensions would provide another avenue to test our machinery.

VII. ACKNOWLEDGMENTS

We thank Kai Phillip Schmidt for insightful discussion on the model Hamiltonian. We thank Anton Montag for the discussions on confirming the emergence of exceptional points in our system. We also thank Jan Alexander Koziol for enriching discussions on the numerical implementation of the local energy. L.W. and F.K.K. acknowledge funding from the Max Planck Society Lise Meitner Excellence Program 2.0.

VIII. DATA AVAILABILITY

The data and codes that support the findings of this study are available from the corresponding author upon reasonable request.

Appendix A: Effect of Boundary Conditions

The analysis presented in Sec. II to Sec. V of this paper was conducted considering PBCs. As predicted in Ref. [16], we show here that PT symmetry is broken as soon as one turns on the non-Hermiticity ($\xi \neq 0$) under PBCs (see Fig. 8). In contrast, Fig. 7 shows that under OBCs, this phase transition is not immediate and only occurs later at some particular values of the NH perturbation.

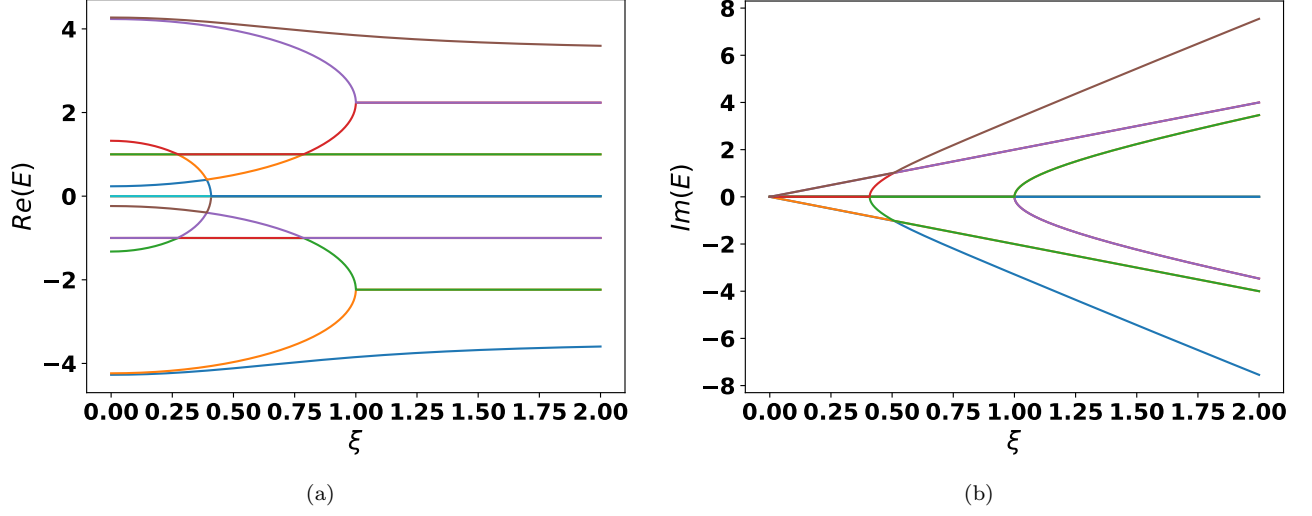


Figure 8: **Energy spectrum under PBCs.** We plot the (a) real and the (b) imaginary parts of the ground state energy under PBCs for $\eta = 0.5$. One enters the broken PT -symmetric regime as soon as one turns on the non-Hermiticity, $\xi \neq 0$. We consider $N = 4$ and the coloring is determined by the order in which the bands appear.

Appendix B: Local Energy and Algorithms

1. Local Energy

The local energy, $E_{\text{loc}}(\mathbf{x})$ in Eq. (4) with \mathbf{x} being the spin configuration, plays a crucial role in the VMC methods, as it provides an efficient way to estimate the expectation value of the Hamiltonian H in a given quantum state. It is defined as the ratio of the Hamiltonian's action on the wavefunction to the wavefunction itself, evaluated at a specific configuration \mathbf{x} .

In non-Hermitian systems, where the left and right eigenstates of the Hamiltonian are distinct, the local energy can be computed using either the right eigenstate $|\Psi_{0,R}\rangle$ or the left eigenstate $\langle\Psi_{0,L}|$, as shown in Eq. (4). Importantly, despite the NH nature of the system, this formulation ensures that the energy remains consistent, whether the Hamiltonian acts from the left or the right. This property makes our formulation of the local energy particularly useful for numerical simulations, as it allows for a meaningful energy evaluation even when conventional Hermitian approaches fail. From the biorthogonality relation in Eq. (2), the ground-state energy of the Hamiltonian is

$$E_0 = \langle H \rangle_0 = \frac{\langle \Psi_{0,L} | H | \Psi_{0,R} \rangle}{\langle \Psi_{0,L} | \Psi_{0,R} \rangle}. \quad (\text{B1})$$

By using the completeness of the spin basis and the fact that $\Psi_R(\mathbf{x}) = \langle \mathbf{x} | \Psi_R \rangle$ or $\Psi_L(\mathbf{x}) = \langle \Psi_L | \mathbf{x} \rangle$ one finds

$$\begin{aligned} \langle H \rangle &= \frac{\sum_{\mathbf{x}} \langle \Psi_{0,L} | \mathbf{x} \rangle \langle \mathbf{x} | H | \Psi_{0,R} \rangle}{\sum_{\mathbf{x}} \langle \Psi_{0,L} | \mathbf{x} \rangle \langle \mathbf{x} | \Psi_{0,R} \rangle} \\ &= \frac{\sum_{\mathbf{x}} \Psi_{0,L}(\mathbf{x}) \left[\frac{\langle \mathbf{x} | H | \Psi_{0,R} \rangle}{\langle \mathbf{x} | \Psi_{0,R} \rangle} \right] \Psi_{0,R}(\mathbf{x})}{\sum_{\mathbf{x}} \Psi_{0,L}(\mathbf{x}) \Psi_{0,R}(\mathbf{x})}. \end{aligned} \quad (\text{B2})$$

The local energy is then taken to be

$$E_{\text{loc}}(\mathbf{x}) = \frac{\langle \mathbf{x} | H | \Psi_{0,R} \rangle}{\langle \mathbf{x} | \Psi_{0,R} \rangle}, \quad (\text{B3})$$

where the summation of these energies becomes the true ground-state energy provided a good approximation of the ansatz. The expression of $E_{\text{loc}}(\mathbf{x})$ in terms of $\langle \Psi_{0,L} |$ can be found in a similar fashion.

2. Algorithms

Recurrent Neural Network (RNN) training

- 1: Initial random spin configuration: \mathbf{x}
 - 2: Initial random RNN ansatz: rnn
 - 3: **for** it in range($steps$) **do**
 - 4: $\mathbf{x} = \text{Autoregressive sampling with RNN}$
 - 5: $\log \Psi(\mathbf{x}) = rnn(\mathbf{x})$
 - 6: $E_{\text{loc}}(\mathbf{x}) = \text{compute_eloc}(\mathbf{x}, \log \Psi(\mathbf{x}))$ with Eq. (B3)
 - 7: $loss_real = \langle \log \Psi(\mathbf{x}) | Re(E_{\text{loc}}(\mathbf{x})) - \log \Psi(\mathbf{x}) | Re(E_{\text{loc}}(\mathbf{x})) \rangle$
 - 8: $grad = \text{gradient}(loss_real, rnn)$
 - 9: Update rnn parameters with gradient descent.
 - 10: **end for**
-

Restricted Boltzmann Machine (RBM) training

- 1: Initial random spin configuration: \mathbf{x}
- 2: Initial random RBM ansatz: rbm
- 3: **for** it in range($steps$) **do**
- 4: $\mathbf{x} = \text{Gibbs sampling with RBM}$

```

5:  log  $\Psi(\mathbf{x}) = \text{rbm}(\mathbf{x})$ 
6:   $E_{\text{loc}}(\mathbf{x}) = \text{compute\_eloc}(\mathbf{x}, \log \Psi(\mathbf{x}))$  with
   Eq. (B3)
7:   $\text{loss\_real} = (\log \Psi(\mathbf{x}) \text{Re}(E_{\text{loc}}(\mathbf{x})) - \log \Psi(\mathbf{x}) \langle \text{Re}(E_{\text{loc}}(\mathbf{x})) \rangle)$ 
8:   $\text{grad} = \text{gradient}(\text{loss\_real}, \text{rbm})$ 
9:  Update rbm parameters with gradient descent.
10: end for

```

Multilayer Perceptron (MLP) training

```

1: Initial random spin configuration:  $\mathbf{x}$ 
2: Initial random MLP ansatz: mlp
3: for it in range(steps) do
4:    $\mathbf{x} = \text{Metropolis sampling with MLP}$ 
5:   log  $\Psi(\mathbf{x}) = \text{mlp}(\mathbf{x})$ 
6:    $E_{\text{loc}}(\mathbf{x}) = \text{compute\_eloc}(\mathbf{x}, \log \Psi(\mathbf{x}))$  with
   Eq. (B3)
7:    $\text{loss\_real} = (\log \Psi(\mathbf{x}) \text{Re}(E_{\text{loc}}(\mathbf{x})) - \log \Psi(\mathbf{x}) \langle \text{Re}(E_{\text{loc}}(\mathbf{x})) \rangle)$ 
8:    $\text{grad} = \text{gradient}(\text{loss\_real}, \text{mlp})$ 
9:   Update mlp parameters with gradient descent.
10: end for

```

Appendix C: Extrapolation of the Series Expansion

The ground-state energy per spin of the NH TFIM at low- ($\eta/J, \xi/J \ll 1$) and high-field ($\eta/J, \xi/J \gg 1$) was derived in Ref. [16], and is given by

$$\begin{aligned}
E_{\text{low}}^{(\eta, \xi)} = & -J - \frac{\eta^2 - \xi^2}{4J} - \frac{\eta^4 + \xi^4}{64J^3} - \frac{5\eta^2\xi^2}{32J^3} - \frac{\eta^6 - \xi^6}{256J^5} \\
& - \frac{7(\eta^4\xi^2 - \eta^2\xi^4)}{256J^5} - \frac{25(\eta^8 + \xi^8)}{16384J^7} - \frac{129(\eta^6\xi^2 + \eta^2\xi^6)}{4096J^7} \\
& - \frac{171\eta^4\xi^4}{8192J^7} - \frac{49(\eta^{10} - \xi^{10})}{65536J^9} + \frac{781(\eta^8\xi^2 - \eta^2\xi^8)}{65536J^9} \\
& - \frac{33(\eta^6\xi^4 - \eta^4\xi^6)}{32768J^9} - \frac{441(\eta^{12} + \xi^{12})}{1048576J^{11}} \\
& - \frac{7631(\eta^{10}\xi^2 + \eta^2\xi^{10})}{524288J^{11}} - \frac{18551(\eta^8\xi^4 + \eta^4\xi^8)}{1048576J^{11}} \\
& - \frac{7241\eta^6\xi^6}{262144J^{11}}, \quad (C1)
\end{aligned}$$

and

$$\begin{aligned}
E_{\text{high}}^{(\eta, \xi)} = & -\eta - \frac{J^2}{4\eta} - \frac{J^4(\eta^2 - 3\xi^2)}{64\eta^3(\eta^2 + \xi^2)} - \frac{J^6(\eta^2 + 5\xi^2)}{256\eta^5(\eta^2 + \xi^2)} \\
& - \frac{J^8(25\eta^6 - 269\eta^4\xi^2 - 405\eta^2\xi^4 - 175\xi^6)}{16384\eta^7(\eta^2 + \xi^2)^3} \\
& - \frac{J^{10}(49\eta^6 + 715\eta^4\xi^2 + 1043\eta^2\xi^4 + 441\xi^6)}{65536\eta^9(\eta^2 + \xi^2)^3}, \quad (C2)
\end{aligned}$$

respectively.

The procedure for extrapolating the SE method in the intermediate-field regime so that these energies can be

used to predict what happens involves a form of fitting. First, we choose to study the system within the range $\eta \in [0, 3]$ with $\xi = \eta/10$, where we reiterate we set $J = 1$. We then subdivide this interval into two parts, where we naively define the low-field regime as $\eta \leq 1.5$ and the high-field regime as $\eta > 1.5$. Next, we plot $E_{\text{low}}^{(\eta, \xi)}$ as a function of $\eta \in [0, 1.5]$ and $E_{\text{high}}^{(\eta, \xi)}$ as a function of $\eta \in [1.5, 3]$ with a step size of 0.1. We observe that around $\eta \approx 1.0$, the energy values of both the low- and high-field regimes begin to increase (see Fig. 9). Indeed, as seen in Fig. 9, for $\eta \leq 1$, $E_{\text{low}}^{(\eta, \xi)}$ remains energetically lower, i.e., below $E_{\text{high}}^{(\eta, \xi)}$, but when $\eta > 1$, $E_{\text{low}}^{(\eta, \xi)}$ becomes energetically higher. The same behavior is observed for $E_{\text{high}}^{(\eta, \xi)}$ when extrapolating backward. Assuming minimal energy in both regimes, we can infer that the low- (high-) field energy remains valid while minimizing energy up to approximately $\eta \approx 1$. Furthermore, beyond $\eta \approx 1$, $E_{\text{low}}^{(\eta, \xi)}$ ceases to exhibit the expected quadratic behavior and instead becomes linear. Similarly, for $E_{\text{high}}^{(\eta, \xi)}$, when fitted backward from $\eta = 3$, the expected linear behavior in this regime breaks down around $\eta \approx 1.0$ and transitions into a quadratic form, suggesting that the regime transition occurs at this point.

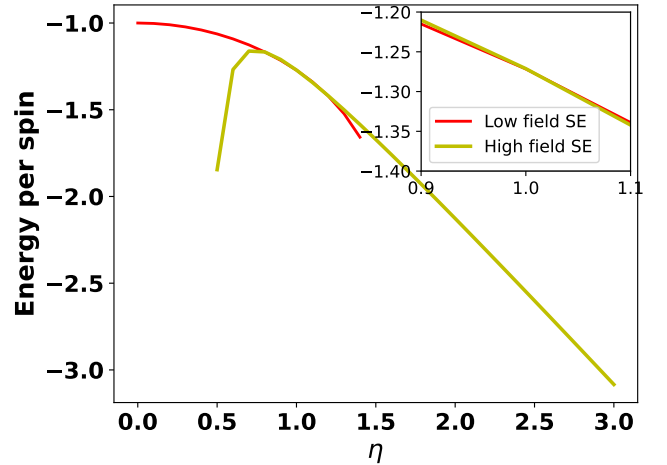


Figure 9: **SE extrapolation.** We extrapolate the SE to capture the intermediate-field regime. For both the low- and high-field regime, we remain in the region of minimal energy.

Appendix D: Enforcing *PT* Symmetry on the Ansätze

In this section, we show how to enforce *PT* symmetry in our neural network architectures. For illustration we show the implementation for an RNN. However, this implementation is valid for both MLP and RBM as well.

In what follows, we propose an implementation of the RNN depicted in Fig. 10 that we use to find the ground-state properties of our model. We employ the approach

described in Secs. II and III and as well as a method similar to the one describe in Ref. [23]. The goal is to enforce a PT -symmetric RNN ansatz $|\Psi_{RNN}\rangle$. Parity P reflects the spatial coordinates or swaps components of a state. In a spin chain, P exchange the i^{th} spin with the $N-i+1^{th}$. Time reversal T complex conjugates the wavefunction or parameters of the ansatz. The PT symmetry is imposed on the RNN ansatz by requesting

$$|\Psi_{RNN}(\mathbf{x}_s)\rangle = T|\Psi_{RNN}(P\mathbf{x}_s)\rangle, \quad (D1)$$

and then symmetrizing the neural network to output

$$|\Psi_{RNN}(\mathbf{x}_s)\rangle = \frac{1}{2} [F(\mathbf{x}_s) + F^*(P\mathbf{x}_s)], \quad (D2)$$

where $F(\mathbf{x}_s)$ is the neural network's unregularized output and \mathbf{x}_s the sampled spin configuration.

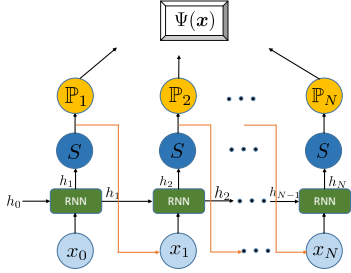


Figure 10: **RNN wavefunction.** The algorithm is fed with some spin configuration x_i (light blue circles) and returns the probability distribution \mathbb{P}_i (yellow circles) of that configuration, which then contributes to the final wavefunction. The green boxes represent the stacked RNN cells, and the dark blue circles are the *Softmax* activation functions.

For a system of N spins, let the probability distribution of the system distributed over a discrete sample space be given by \mathbb{P} . Let a single walker or a single snapshot of the system's states be given by a spin configuration $\mathbf{x} = (x_1, x_2, x_3, \dots, x_N)$. The probability for finding a spin in a particular configuration \mathbf{x}_i influences the probability of finding a spin in one of the remaining configurations $\mathbf{x}_j = \mathbf{x} - \{\mathbf{x}_i\}$, such that

$$\mathbb{P}(\mathbf{x}) = \prod_{j < i=1}^N \mathbb{P}(\mathbf{x}_i | \mathbf{x}_j), \quad (D3)$$

where $\mathbb{P}(\mathbf{x}_i | \mathbf{x}_j)$ is the conditional probability distribution of \mathbf{x}_i provided \mathbf{x}_j are known. The probability in Eq. (D3) is computed by the RNN cell and one can simply extract the wavefunction (see Fig. 10) of the system from this probability by taking the sum of the “square roots” as follows

$$|\Psi(\mathbf{x})\rangle = \sum_{\mathbf{x}} \sqrt{P(\mathbf{x})} |\mathbf{x}\rangle. \quad (D4)$$

Initially, the neural network takes as input some random spin \mathbf{x}_0 and hidden state h_0 . Then one applies the *Softmax* non-linear function to ensure that the network output has a probabilistic behavior (see Fig. 10). Once the *Softmax* is applied, one obtains a new spin configuration \mathbf{x}_1 and a probability amplitude or weight ω_1 such that the probability at the first step is $P_1 = \omega_1 \mathbf{x}_1$. The new hidden state h_1 from this first iteration together with \mathbf{x}_1 are fed as input in the next step, and the process is repeated until the VMC recovers an energy that converges to the true ground state of the system. This is the so-called auto-regressive property of RNN. The interested reader is referred to Refs. [58, 59] for more information about RNN. It is instructive to note that, provided the ubiquitous occurrence of complex-valued wavefunctions in physical systems, one can easily adapt the RNN in Fig. 10 to capture the complex part (phase) of the wavefunction. In this case, the RNN is designed to return both the real and imaginary parts of the wavefunction [23].

Appendix E: Simulation Parameters

RBM parameters	Entries
Optimizer	Adam
Seed	111
Input dimension	2
Sampling	Gibbs
Coupling J	1
System size	[10,100]
Learning rate	10^{-2}
Number of hidden units	34
Number of layers	1
Number of samples	1024
Training steps	10^3
Ansatz	PT -sym RBM
Magnetic field component	$\xi = \eta/10$
Offset in the log probability	10^{-15}
Regularization factor of the cost function α	0.1

Table I: **Restricted Boltzmann Machine.** Data used for all simulations with RBM.

RNN parameters	Entries
Optimizer	Adam
RNN cell	Vanilla/GRU
Seed	111
Input dimension	2
Sampling	VMC
Coupling J	1
System size	[10,100]
Activation function	tanh/Softmax
Learning rate	10^{-2}
Number of hidden units	34
Number of layers	1
Number of samples	1024
Training steps	10^3
Ansatz	<i>PT</i> -sym pRNN
Magnetic field component	$\xi = \eta/10$
Offset in the log probability	10^{-15}
Regularization factor of the cost function α	0.1

Table II: **Recurrent neural network**. Data used for all simulations with RNN.

MLP parameters	Entries
Optimizer	Adam
Seed	111
Input dimension	2
Sampling	Metropolis
Activation function	Relu
Coupling J	1
System size	[10,100]
Learning rate	10^{-2}
Number of hidden units	34
Number of layers	1
Number of samples	1024
Training steps	10^3
Ansatz	<i>PT</i> -sym MLP
Magnetic field component	$\xi = \eta/10$
Offset in the log probability	10^{-15}
Regularization factor of the cost function α	0.1

Table III: **Multilayer Perceptrons**. Data used for all simulations with MLP.

-
- [1] Y. Ashida, Z. Gong, and M. Ueda, *Advances in Physics* **69**, 249 (2020).
- [2] E. J. Bergholtz, J. C. Budich, and F. K. Kunst, *Reviews of Modern Physics* **93**, 015005 (2021).
- [3] C. M. Bender and S. Boettcher, *Physical Review Letters* **80**, 5243 (1998).
- [4] R. El-Ganainy, K. G. Makris, M. Khajavikhan, Z. H. Musslimani, S. Rotter, and D. N. Christodoulides, *Nature Physics* **14**, 11 (2018).
- [5] M. Ateuafack, L. Wah, M. Jipdi, J. N. Kuetche, L. Temdie, J. Difo, and L. Fai, *Physics Letters A* **533**, 130216 (2025).
- [6] Y. Zhang and Z. Wei, *Laser & Photonics Reviews* **19**, 2400099 (2024).
- [7] S. K. Özdemir, S. Rotter, F. Nori, and L. Yang, *Nature Materials* **18**, 783 (2019).
- [8] J. Li, A. K. Harter, J. Liu, L. de Melo, Y. N. Joglekar, and L. Luo, *Nature Communications* **10**, 855 (2019).
- [9] Z. Ren, D. Liu, E. Zhao, C. He, K. K. Pak, J. Li, and G.-B. Jo, *Nature Physics* **18**, 385 (2022).
- [10] L. Ding, K. Shi, Q. Zhang, D. Shen, X. Zhang, and W. Zhang, *Phys. Rev. Lett.* **126**, 083604 (2021).
- [11] J. T. Gohsrich, A. Banerjee, and F. K. Kunst, *Europhysics Letters* (2025).
- [12] D. J. Luitz and F. Piazza, *Phys. Rev. Res.* **1**, 033051 (2019).
- [13] D.-W. Zhang, Y.-L. Chen, G.-Q. Zhang, L.-J. Lang, Z. Li, and S.-L. Zhu, *Phys. Rev. B* **101**, 235150 (2020).
- [14] C.-Z. Lu, X. Deng, S.-P. Kou, and G. Sun, *Physical Review B* **110**, 014441 (2024).
- [15] G. Sun, J.-C. Tang, and S.-P. Kou, *Frontiers of Physics* **17**, 33502 (2021).
- [16] L. Lenke, M. Mühlhauser, and K. P. Schmidt, *Physical Review B* **104**, 195137 (2021).
- [17] C. Li, G. Zhang, X. Zhang, and Z. Song, *Physical Review A* **90**, 012103 (2014).
- [18] E. M. Guerra, I. Gornyi, and Y. Gefen, arXiv preprint arXiv:2502.07775 (2025).
- [19] M. Krenn, J. Landgraf, T. Foessel, and F. Marquardt, *Physical Review A* **107**, 010101 (2023).
- [20] G. Carleo, I. Cirac, K. Cranmer, L. Daudet, M. Schuld, N. Tishby, L. Vogt-Maranto, and L. Zdeborová, *Reviews of Modern Physics* **91**, 045002 (2019).
- [21] J. Carrasquilla, *Advances in Physics: X* **5**, 1797528 (2020).
- [22] G. Carleo and M. Troyer, *Science* **355**, 602 (2017).
- [23] M. Hibat-Allah, M. Ganahl, L. E. Hayward, R. G. Melko, and J. Carrasquilla, *Physical Review Research* **2**, 023358 (2020).
- [24] S. Pilati, E. Inack, and P. Pieri, *Physical Review E* **100**, 043301 (2019).
- [25] E. Inack, G. Santoro, L. Dell’Anna, and S. Pilati, *Physical Review B* **98**, 235145 (2018).
- [26] H. Taud and J.-F. Mas, in *Geomatic approaches for modeling land change scenarios* (Springer, 2017) pp. 451–455.
- [27] O. Sharir, Y. Levine, N. Wies, G. Carleo, and A. Shashua, *Physical Review Letters* **124**, 020503 (2020).
- [28] E. Ibarra-García-Padilla, H. Lange, R. G. Melko, R. T. Scalettar, J. Carrasquilla, A. Bohrdt, and E. Khatami, *Physical Review Research* **7**, 013122 (2025).
- [29] F. K. Kunst, E. Edvardsson, J. C. Budich, and E. J. Bergholtz, *Physical Review Letters* **121**, 026808 (2018).
- [30] D. C. Brody, *Journal of Physics A: Mathematical and Theoretical* **47**, 035305 (2013).

- [31] X.-J. Yu, Z. Pan, L. Xu, and Z.-X. Li, *Physical Review Letters* **132**, 116503 (2024).
- [32] Y.-Q. Chen, S.-X. Zhang, C.-Y. Hsieh, and S. Zhang, *Physical Review A* **107**, 042418 (2023).
- [33] J. Carrasquilla and G. Torlai, *PRX Quantum* **2**, 040201 (2021).
- [34] J. Kim, G. Pescia, B. Fore, J. Nys, G. Carleo, S. Gandolfi, M. Hjorth-Jensen, and A. Lovato, *Communications Physics* **7**, 148 (2024).
- [35] M. J. Hartmann and G. Carleo, *Physical Review Letters* **122**, 250502 (2019).
- [36] F. Döschl, F. A. Palm, H. Lange, F. Grusdt, and A. Bohrdt, *Physical Review B* **111**, 045408 (2025).
- [37] H. Lange, A. Van de Walle, A. Abedinnia, and A. Bohrdt, *Quantum Science and Technology* **10**, 1088/2058-9565/ad3f18 (2024).
- [38] Z. Cai and J. Liu, *Physical Review B* **97**, 035116 (2018).
- [39] M. Hibat-Allah, E. Merali, G. Torlai, R. G. Melko, and J. Carrasquilla, arXiv preprint arXiv:2405.20384 (2024).
- [40] L. Medsker and L. C. Jain, *Recurrent neural networks: design and applications* (CRC press, 1999).
- [41] R. Salakhutdinov, A. Mnih, and G. Hinton, in *Proceedings of the 24th international conference on Machine learning* (2007) pp. 791–798.
- [42] R. G. Melko, G. Carleo, J. Carrasquilla, and J. I. Cirac, *Nature Physics* **15**, 887 (2019).
- [43] G. E. Hinton, in *Neural Networks: Tricks of the Trade: Second Edition* (Springer, 2012) pp. 599–619.
- [44] F. Murtagh, *Neurocomputing* **2**, 183 (1991).
- [45] L. B. Almeida, in *Handbook of Neural Computation* (CRC Press, 2020) pp. C1–2.
- [46] R. Kruse, S. Mostaghim, C. Borgelt, C. Braune, and M. Steinbrecher, in *Computational intelligence: a methodological introduction* (Springer, 2022) pp. 53–124.
- [47] M. Reh, M. Schmitt, and M. Gärttner, *Physical Review B* **107**, 195115 (2023).
- [48] L. Torrey and J. Shavlik, in *Handbook of research on machine learning applications and trends: algorithms, methods, and techniques* (IGI global, 2010) pp. 242–264.
- [49] R. Zen, L. My, R. Tan, F. Hébert, M. Gattobigio, C. Miniatura, D. Poletti, and S. Bressan, *Physical Review E* **101**, 053301 (2020).
- [50] R. Zen, L. My, R. Tan, F. Hébert, M. Gattobigio, C. Miniatura, D. Poletti, and S. Bressan, in *ECAI 2020* (IOS Press, 2020) pp. 1962–1969.
- [51] R. Rende, S. Goldt, F. Becca, and L. L. Viteritti, *Physical Review Research* **6**, 043280 (2024).
- [52] P. Pfeuty, *ANNALS of Physics* **57**, 79 (1970).
- [53] D. Pfau, S. Axelrod, H. Sutterud, I. von Glehn, and J. S. Spencer, *Science* **385**, eadn0137 (2024), <https://www.science.org/doi/pdf/10.1126/science.adn0137>.
- [54] K. Choo, G. Carleo, N. Regnault, and T. Neupert, *Physical Review Letters* **121**, 167204 (2018).
- [55] M. T. Entwistle, Z. Schätzle, P. A. Erdman, J. Hermann, and F. Noé, *Nature Communications* **14**, 274 (2023).
- [56] I. Mandal and E. J. Bergholtz, *Phys. Rev. Lett.* **127**, 186601 (2021).
- [57] A. Montag and F. K. Kunst, *Phys. Rev. Res.* **6**, 023205 (2024).
- [58] L. R. Medsker, L. Jain, *et al.*, *Design and Applications* **5**, 2 (2001).
- [59] Y. Yu, X. Si, C. Hu, and J. Zhang, *Neural computation* **31**, 1235 (2019).